RSC Advances

PAPER

View Article Online
View Journal | View Issue

Cite this: *RSC Adv.*, 2023, **13**, 28984

Synergistic activation of persulfate by a manganese cobalt oxide/reduced graphene oxide nanocomposite with enhanced degradation of trichloroethylene†

Lu Zhang,[ab] Pengfei Ji,[a] Rui Song,[a] Jiayuan Li,[a] Kaifeng Qin[b] and Gang Xu *[ab]

Advanced oxidation technology based on persulfate is one of the most reliable and effective technologies for the degradation of wastewater, however the key lies in developing highly efficient catalysts to activate persulfate. Herein, manganese cobalt oxide/reduced graphene oxide ($MnCo_2O_4$/rGO) nanocomposites were successfully synthesized *via* a facile solvothermal method and employed as a highly efficient catalyst to active persulfate for the degradation of trichloroethylene (TCE). The rGO nanosheets have large surface areas, which can increase the contact area with reactants and make the degradation more efficient. Additionally, the $MnCo_2O_4$ nanoparticles are *in situ* grown on the surface of ultrathin rGO nanosheets, endowing the material with high structural porosity and fast transport channels, and are beneficial for the improvement of catalytic sites and the transport of catalysis-relevant species. More importantly, the close contact between $MnCo_2O_4$ nanoparticles and rGO nanosheets synergistically favors the electron transfer, thereby accelerating the electron transfer, improving the activation efficiency, and promoting the generation of sulfate radicals ($\cdot SO_4^-$). rGO can also reduce the spillover of metal ions. The kinetics model and degradation mechanism of the nanocomposites are also proposed.

Received 8th June 2023
Accepted 22nd August 2023

DOI: 10.1039/d3ra03834c

rsc.li/rsc-advances

Introduction

Trichloroethylene (TCE) is a common volatile organic compound (VOC) with unique solvent properties that make it suitable for a wide range of industrial applications.[1] Since the early 20th century, TCE has been widely used as an industrial degreasing solvent, as well as for dry cleaning and food processing, and as a raw material for printing inks and paints, in addition to its use as a general anesthetic or analgesic. Although TCE is not naturally occurring in the environment, it still can be found in underground and surface waters as a result of its manufacture, use, and treatment.[2] However, TCE can pose a serious threat to human health when released into the environment, as it has been shown to be carcinogenic and mutagenic, and can cause chronic diseases such as vertigo, tremors, nausea, fatigue, sleepiness, liver cancer, hepatitis, and heart failure.[3] Therefore, due to its various shortcomings, the importance of TCE treatment cannot be overstated.

Given the widespread prevalence of TCE in the environment and its adverse effects on human health, numerous methods have been developed to remove and decompose TCE from contaminated water, air, and soil media over the past few decades.[4–8] Physical methods can only achieve TCE degradation efficiency of up to about 67%,[9] while biodegradation and chemical methods can achieve a higher efficiency.[10,11] The most commonly used physical methods are adsorption and membrane filtration technology, with activated carbon adsorption technology being developed in the early stages for trichloroethylene.[10] However, physical methods only transfer pollutants from one medium to another without destroying them, which may cause secondary pollution. Biodegradation methods, on the other hand, decompose and transform chlorinated pollutants using the metabolic activities of microorganisms in nature. Biodegradation methods are advantageous as they are low cost, do not produce secondary pollution, but have a long degradation period and difficult temperature control issues that need addressing.[11,12] For chemical methods, it involves adding chemicals to the water to separate pollutants from the water or applying external energy to promote the reaction of pollutants for decomposition. This method includes incineration,[13] photocatalytic oxidation,[14] nano zero valent iron reduction,[15] and advanced oxidation.[16] Although incineration can remove pollutants in a short time, it is costly, requires a large amount of external energy, and produces highly toxic products. Photocatalysts have shortcomings such as a wide band gap energy, low light absorption capacity, and fast

[a]*School of Environmental and Chemical Engineering, Shanghai University, 99 Shangda Road, Shanghai 200444, P. R. China. E-mail: xugang@shu.edu.cn*

[b]*Key Laboratory of Organic Compound Pollution Control Engineering, Ministry of Education, Shanghai 200444, P. R. China*

† Electronic supplementary information (ESI) available. See DOI: https://doi.org/10.1039/d3ra03834c

recombination rate, leading to a small number of photo-generated active free radical available for photodegradation at the surface reaction site, hindering practical application. Nano zero-valent iron agglomerates easily, resulting in a sharp decline in reactivity and causing secondary pollution in the repair process, leading to high economic costs. Particularly, advanced oxidation technology is preferred due to its simplicity, environmental compatibility, and versatility.

Recently, reactive persulfate (PS) has received attention in water and wastewater treatment due to its longer half-life, stronger oxidation, higher electrode potential, and wider pH range.[17,18] Compared to the hydroxyl radical, sulfate radicals ($\cdot SO_4^-$) has a more extended half-life (30–40 μs), stronger oxidation, higher electrode potential ($E_0 = 2.6$–3.2 V), and wider pH range (2–8), making the sulfate radical method more effective in degrading TCE in water. In previous research, the oxidation of PS has been shown to rely on the creation of highly active sulfate radicals. These sulfate radicals can be produced through various methods such as thermal treatment,[19–21] photolysis,[22] acoustic activation,[23] radioactive activation,[24] and the reaction of PS with transition metal oxide composites.[25,26] Compared to other methods that require external energy input, a transition metal catalyst can activate persulfate at room temperature and pressure without the need for additional energy. Previous studies have identified divalent cobalt as the most effective catalyst to activate PS.[27,28] For instance, studies by Chen *et al.*[29] and Muhammad *et al.*[30] have used Co_3O_4 as a catalyst to active peroxydisulfate (PDS) to degrade acid orange 7 and phenol. Reduced graphene oxide (rGO) is another effective carrier material for catalytic degradation of pollutants in water. The combination of catalyst and rGO offers numerous advantages, including high surface area and tensile strength, improved electronic conductivity and mobility, lightweight, and high stability.[31,32] However, to our knowledge, few studies have investigated the activation of persulfate by $MnCo_2O_4$/rGO for the degradation of TCE.

Herein, we prepared $MnCo_2O_4$/rGO composites using a two-step solvothermal method and employed them as a catalyst to activate persulfate for the degradation of TCE. Benefiting from the merits of structure and composites of the as-prepared sample, including large surface area, high structural porosity, fast transport channels, and the synergistic effect between $MnCo_2O_4$ nanoparticles and rGO nanosheets, enabling the degradation efficiency of TCE to reach 95% within 4 h under the optimal reaction conditions. Additionally, we also studied the degradation efficiency of TCE under different conditions in the reaction system and analyzed the mechanism of $MnCo_2O_4$/rGO activation of persulfate to understand the degradation pathway of TCE.

Experimental section

Reagents and chemicals

Manganese acetate tetrahydrate ($Mn(Ac)_2 \cdot 4H_2O$) and cobalt acetate tetrahydrate ($Co(Ac)_2 \cdot 4H_2O$) were purchased from Aladdin Biochemical Technology Co., LTD. Potassium persulfate ($K_2S_2O_4$), purchased from Macklin Co., LTD. Trichloroethylene (TCE), ammonium fluoride (NH_4F), graphite powder (C), potassium permanganate ($KMnO_4$), sodium nitrate ($NaNO_3$), hydrogen peroxide (H_2O_2), ethanol (99.5%), ethylene glycol (99.7%), sulfuric acid were purchased from Sinopharm Chemical Reagent Co., LTD. All reagents were used without further purification.

Synthesis of manganese cobalt oxide ($MnCo_2O_4$) nanoparticle

The $MnCo_2O_4$ nanoparticles were prepared *via* a solution-based method. Typically, 1.471 g of $Mn(Ac)_2 \cdot 4H_2O$ and 2.989 g of $Co(Ac)_2 \cdot 4H_2O$ were added to 45 mL ethylene glycol and 15 mL de-ionized water with stirring for 5 min. Then, 1.34 g of NH_4F was added into the above solution with continue stirring for 2 h. After that, the mixture was transferred to a 100 mL Teflon-lined autoclave and kept at 180 °C for 16 h. Being cooled to ambient temperature, the resulting mixture was centrifugalized and the solids were washed with de-ionized water and ethanol for several times, and dried under vacuum at 80 °C for 16 h. Finally, the resulting product was calcined in Muffle furnace at 400 °C for 2 h at a heating rate of 2 °C min^{-1}.

Synthesis of $MnCo_2O_4$/rGO nanocomposite

To prepare $MnCo_2O_4$/rGO nanocomposite, graphene oxide (GO) was firstly prepared by the modified Hummers' method.[33] Then, 30, 60, 90 mg of the as-prepared GO was added into a mixed solvent of 45 mL of ethylene glycol and 15 mL de-ionized water with ultrasonic treatment to form a GO solution. Subsequently, 1.0 g of $MnCo_2O_4$ was added into the GO solution with stirring for 2 h. The mixture was transferred to a 100 mL Teflon-lined autoclave and kept at 180 °C for 10 h. After cooling to room temperature, the product of $MnCo_2O_4$/rGO nanocomposite was collected by centrifugation and washed with de-ionized water and ethanol for several times and finally dried under vacuum at 80 °C for 24 h.

Experimental procedure

To simulate the dark conditions of groundwater, all catalytic degradation studies were performed in a 250 mL beaker in the dark. The beaker contained 200 mL of 0.15 mM TCE solution. A mechanical stirring arm was used to stir the solution and sample it at a certain time (1, 2, 3, 4 h) at room temperature. The pH of aqueous solution of TCE was adjusted with dipotassium hydrogen phosphate (pH = 9, 11) and sulfuric acid (pH = 3). Then, a certain amount (0.05, 0.1, 0.2, 0.3, 0.4 g L^{-1}) of $MnCo_2O_4$/rGO composite material and PS were added to the solution for reaction. Samples of 3 mL were taken at fixed intervals and filtered (0.22 μm membrane) to obtain the samples to be tested.

In order to verify the efficient degradation of TCE by $MnCo_2O_4$/rGO/PS, the degradation efficiency of TCE by $MnCo_2O_4$, $MnCo_2O_4$/rGO, PS, $MnCo_2O_4$/PS and $MnCo_2O_4$/rGO/PS was compared. The factors such as the amount of catalyst, the amount of PS, the initial pH and the presence of anions were investigated to optimize the activation conditions of $MnCo_2O_4$/rGO/PS system. In order to evaluate the stability and reusability of the catalyst, the $MnCo_2O_4$/rGO nanocomposite is

centrifugally collected after each reaction, cleaning with ethanol and DI water, then dried in the drying oven. In order to investigate the reaction mechanism, two different free radical scavengers were used to determine the type of free radicals formed in the $MnCo_2O_4$/rGO/PS system. All the above experiments were performed three times and the results were averaged.

To get insights into the degradation pathway and mechanism, the concentration of TCE and their degradation intermediates was determined using gas chromatography-mass spectrometry (GC-MS) with a purge and capture device, employing a DB-VRX column. Specific GC-MS parameters were employed for the analysis. The purge trap parameters included a purge flow rate of 40 mL min^{-1}, a purge time of 11 min, dry purge time of 1 min, pre-desorption temperature of 180 °C, desorption temperature of 190 °C, desorption time of 2 min, baking temperature of 200 °C, and baking time of 6 min. Shunt injection (30 : 1) was utilized as the injection method for gas chromatography. The inlet temperature was set at 220 °C, and the temperature program was as follows: it was kept at 35 °C for 2 min, then increased to 120 °C at 5 °C min^{-1}, and finally raised to 220 °C at 10 °C min^{-1} for 2 min. Helium was used as the carrier gas with a flow rate of 1 mL min^{-1}. For mass spectrometry, the EI source was employed, with an ion source temperature of 230 °C and an ionization energy of 70 eV. The scanning mode was SIM ion scan, and the solvent delay was set to 2 min. The electron doubling voltage was consistent with the tuning voltage, and the interface temperature was maintained at 280 °C.

Characterization

X-ray diffraction (XRD) patterns of the products were acquired using a D/Max-2004 X-ray powder diffractometer (Bruker, Germany) with 2θ ranging from 10° to 80°. The morphologies and crystal structure of the catalysts were characterized *via* the scanning electron microscope (SEM, ZEISS Sigma 300) and transmission electron microscopy (TEM, JEOL JEM 2100, 200 kV). Brunauer–Emmett–Teller (BET) surface area of the samples were collected by N_2 adsorption–desorption method at 77 K on the ASAP 2010 instrument (Micromeritics ASAP2460). X-ray photoelectron spectra (XPS, Thermo Scientific K-Alpha) was applied to detect the surface elements.

Results and discussion

Microstructural analysis

Fig. 1a displays the XRD patterns of the as-synthesized rGO, $MnCo_2O_4$, and $MnCo_2O_4$/rGO composites. The (002) peak of rGO shows broadening and reduced intensity, indicating the formation of a highly disordered and defect-rich structure in the nanosheets. The cubic phase of $MnCo_2O_4$ is characterized by lattice constants of $a = b = c = 8.269$ Å (JCPDS no. 23-1237), and the diffraction peaks at 2θ of 18.3°, 30.2°, 35.6°, 37.00°, 43.2°, 57.2°, and 62.7° correspond to the (111), (220), (311), (222), (400), (511), and (440) planes. It confirms the spinel structure of $MnCo_2O_4$/rGO. Coupling $MnCo_2O_4$ with rGO does not affect the diffraction peaks of $MnCo_2O_4$, which remain clear and show a similar XRD pattern to that of $MnCo_2O_4$. Notably, rGO shows no distinct diffraction peaks due to the low quantity and relatively low diffraction intensity of rGO nanosheets. These results suggest the successful synthesis of $MnCo_2O_4$/rGO composites. Additionally, the Scherrer formula estimated the average grain size of $MnCo_2O_4$ nanoparticles to be within the range of 4.5 nm, consistent with the TEM result presented below.

The FT-IR spectra of $MnCo_2O_4$ and $MnCo_2O_4$/rGO are presented in Fig. 1b. The observed peaks at approximately 3600 cm^{-1}, 1600 cm^{-1}, 1300 cm^{-1}, and 1200 cm^{-1} can be attributed to residual oxygen and structural defects on the rGO. Furthermore, two distinct and sharp absorption bands at 551 cm^{-1} and 638 cm^{-1} are observed, originating from the stretching vibrations of the metal–oxygen bonds. Specifically, the 542 cm^{-1} (ν_o) band corresponds to the Co^{3+}/Mn^{3+} vibrations in the O_h complexes, while the 629 cm^{-1} (ν_t) band is associated with the Co^{2+} vibrations in the T_d complexes of the spinel lattice.

The Raman spectra of $MnCo_2O_4$/rGO are depicted in Fig. 1c, illustrating the characteristic bands known as the G band and D band, which originate from carbon vibrations. The D band, observed at 1355 cm^{-1}, exhibits symmetry with A_{1g} and corresponds to photons near the boundary of the K region. The peak at 1598 cm^{-1} signifies the composite structure of rGO nanosheets, with the corresponding Raman active state of the G band identified as E_{2g}. Moreover, the Raman mode at approximately 691 cm^{-1} (A_{1g}) can be attributed to the distinctive

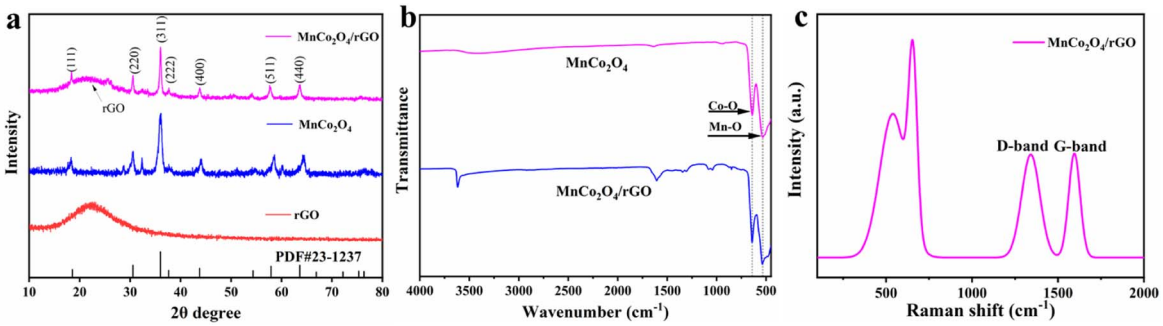

Fig. 1 (a) XRD patterns of the as-synthesized rGO, $MnCo_2O_4$ and $MnCo_2O_4$/rGO samples; (b) FT-IR spectroscopy of $MnCo_2O_4$ and $MnCo_2O_4$/rGO samples; (c) Raman spectroscopy of $MnCo_2O_4$/rGO sample.

characteristics of octahedral (Co–O_6) sites, while the mode at around 533 cm^{-1} (F^3_{2g}) corresponds to tetrahedral (Co–O_4) sites.[34] These results confirm the successful synthesis of the $MnCo_2O_4$/rGO compound.

The morphology and microstructure of $MnCo_2O_4$ and $MnCo_2O_4$/rGO nanocomposites were analyzed in detail using field emission scanning electron microscopy (FESEM) and transmission electron microscopy (TEM). SEM images (Fig. 2a and b) revealed the spinel structure of $MnCo_2O_4$ nanoparticles. Lattice fringes were observed in the TEM images (Fig. 2c and d). The SEM images in Fig. 2e and f demonstrated that the $MnCo_2O_4$/rGO nanocomposites consisted of rGO nanosheets and $MnCo_2O_4$ nanoparticles. The TEM image in Fig. 2g further confirmed the presence of irregular sheet-like morphologies and the existence of rGO in the sample. A high-resolution TEM image (Fig. 2h) showed that $MnCo_2O_4$ nanoparticles were deposited on the surface of rGO nanosheets, which can reduce the restacking of rGO nanosheets and increase the contact area with reactants, resulting in better catalytic performance. The $MnCo_2O_4$ nanoparticles exhibited high crystallinity, as confirmed by the clear lattice fringes with *d*-spacings of 0.249 nm corresponding to the (311) planes of $MnCo_2O_4$ (Fig. 2h). The EDX results (Fig. 2i) indicated the presence of Mn, Co, C, and O elements in the sample, with a relatively uniform distribution.

BET analysis

By analyzing the N_2 adsorption and desorption isotherms and the pore-size distribution of the as-synthesized $MnCo_2O_4$ and $MnCo_2O_4$/rGO samples, the BET surface area and detailed pore structure were determined (Fig. 3). It was found that the $MnCo_2O_4$/rGO sample has a larger BET specific surface area of 43.9 $m^2\ g^{-1}$ than that of pristine $MnCo_2O_4$ nanoparticles (35.7 $m^2\ g^{-1}$). Additionally, the pore volume of the $MnCo_2O_4$/rGO sample (0.27 $cm^3\ g^{-1}$) is also larger than the bare $MnCo_2O_4$ nanoparticles (0.21 $cm^3\ g^{-1}$). These results indicate that the RGO layer is flaked and wrinkled due to the insertion of $MnCo_2O_4$ nanoparticles, leading to an increase in specific surface area and the formation of micro-mesoporous pores.

Degradation performance

Catalytic evaluation. The as-synthesized $MnCo_2O_4$/rGO composite was utilized as a highly efficient catalyst to activate persulfate for TCE degradation. The degradation of TCE was investigated under different reaction conditions, and the TCE concentration changes were recorded, as shown in Fig. 4a. It was observed that $MnCo_2O_4$ had no discernible effect on TCE degradation without the addition of persulfate, whereas $MnCo_2O_4$/rGO showed a certain degree of degradation effect. This can be attributed to the presence of rGO, which can react

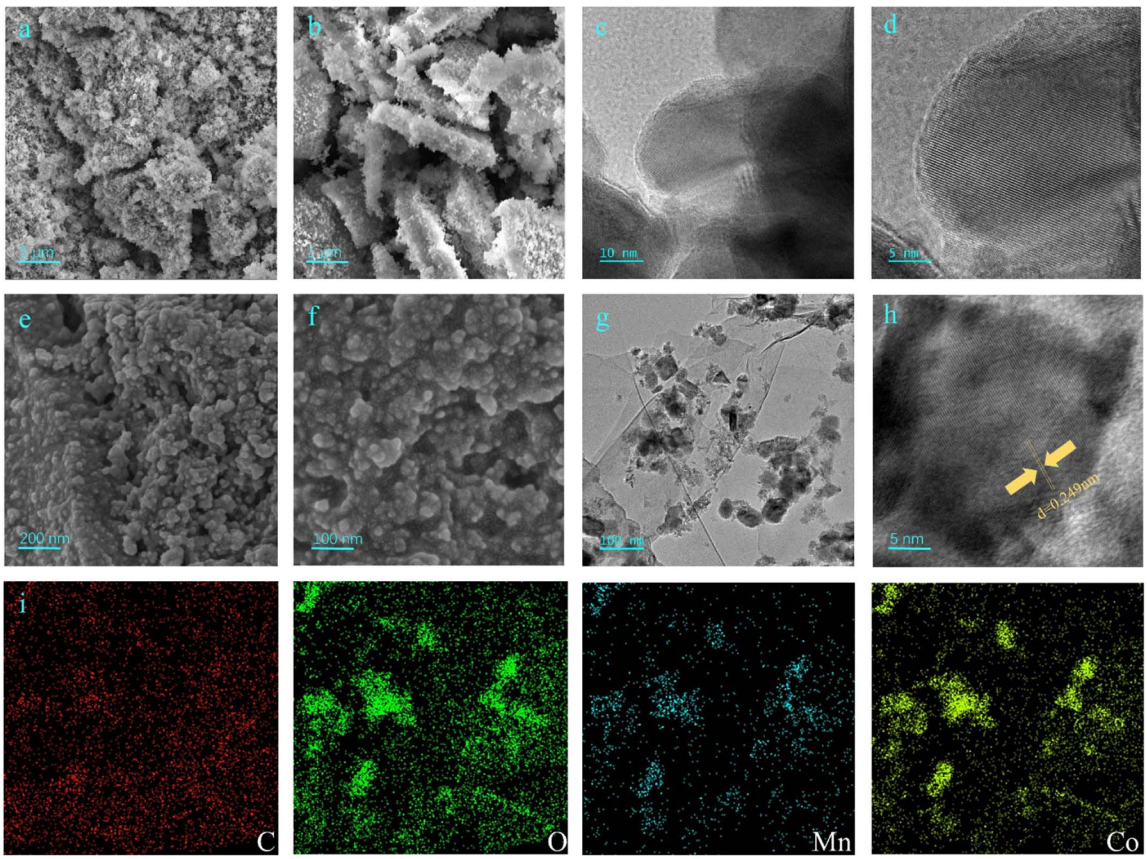

Fig. 2 SEM (a) and (b), TEM (c) and HRTEM (d) images of $MnCo_2O_4$ nanoparticle, SEM (e) and (f), TEM (g), HRTEM (h) and STEM-EDX (i) images of the as-synthesized $MnCo_2O_4$/rGO nanocomposite.

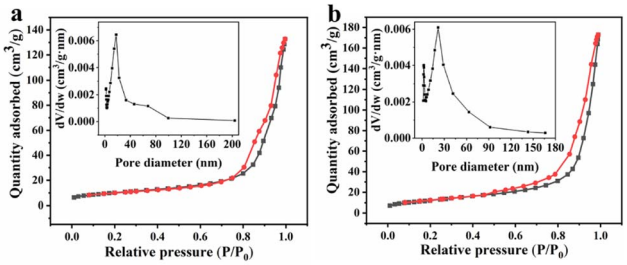

Fig. 3 Nitrogen adsorption–desorption isotherm plots of (a) $MnCo_2O_4$ and (b) $MnCo_2O_4$/rGO and BJH pore distribution (inset).

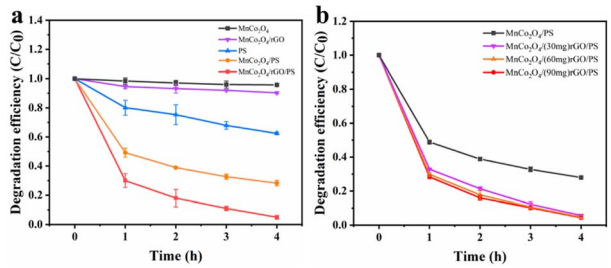

Fig. 4 Degradation efficiency of TCE in different systems (a) and effect of rGO loading on TCE degradation (b) [reaction conditions: persulfate concentration = 0.3 g L^{-1}, catalyst dosage = 0.3 g L^{-1}, reaction temperature = 25 °C and initial pH value = 6 (unadjusted)].

with TCE and promote its degradation.[32] In contrast, persulfate alone degraded only 40% of TCE after a reaction time of 4 h. However, when $MnCo_2O_4$ was added, the TCE degradation efficiency was significantly improved, reaching 71%, indicating that persulfate can be effectively activated by Mn(II) and Co(III). Moreover, the use of $MnCo_2O_4$/rGO as a catalyst further enhanced the TCE degradation efficiency to 95%. This enhanced efficiency can be attributed to the higher electron mobility of rGO and the larger specific surface area of the composite, which expose more active sites and thus improve the reaction efficiency.[35]

Effects of rGO loading. Firstly, the degradation efficiency of $MnCo_2O_4$/rGO composites prepared with different rGO loads (30, 60, 90 mg) was investigated. As shown in Fig. 4b, the degradation efficiency reached 94.3%, 95.1% and 95.5% respectively after 4 hours. It can be seen that the load of rGO has little effect on the degradation efficiency. When the load of rGO is 30 mg, the degradation efficiency is increased because rGO improves the electron transfer rate. When the loading capacity of rGO is 60 mg and 90 mg, the degradation efficiency is further improved due to the adsorption and interaction of $MnCo_2O_4$/rGO. In order to avoid incomplete degradation caused by excessive adsorption of rGO on TCE, 60 mg of rGO was selected to be combined with $MnCo_2O_4$.

Effects of catalyst dosage. To maximize the degradation efficiency, the dosage of catalysts was optimized. Fig. 5a illustrates the impact of different amounts of $MnCo_2O_4$/rGO on TCE degradation at a constant persulfate concentration. It is evident that the degradation efficiency of TCE increases significantly

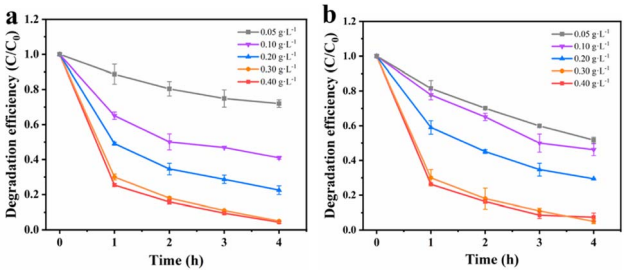

Fig. 5 Effect of reaction parameters on TCE degradation: (a) catalyst dosage [PS dosage = 0.3 g L^{-1}] and (b) PS dosage [catalyst dosage = 0.3 g L^{-1}] [reaction conditions: reaction temperature = 25 °C and initial pH value = 6 (unadjusted)].

with higher dosages of $MnCo_2O_4$/rGO. At a dosage of 0.3 g L^{-1}, the degradation efficiency reaches its maximum, approximately 95%, due to the increased number of active sites available for the reaction.[36] Notably, even at a dosage of 0.4 g L^{-1}, the degradation efficiency continues to increase. The higher dosage results in a greater number of active sites, thereby enhancing the degradation efficiency. To balance economic considerations and minimize metal spillover, a catalyst dosage of 0.3 g L^{-1} was selected as the optimal reaction condition.

Effects of PS dosage. Previous studies have shown that the concentration of persulfate has a significant impact on the removal of target substances during reactions. As a sequence, the degradation efficiency of TCE in the $MnCo_2O_4$/rGO/PS system at various persulfate concentrations (0.05, 0.1, 0.2, 0.3, and 0.4 g L^{-1}) was investigated. As depicted in Fig. 5b, when the $MnCo_2O_4$/rGO dosage is 0.3 g L^{-1}, the degradation efficiency of TCE increases from 21% to 95% with the increase in persulfate concentration. This suggests that higher persulfate concentrations lead to better degradation of TCE. However, at higher concentrations, the increase can inhibit the removal of the target due to the recombination of excess $\cdot SO_4^-$ and the self-depletion caused by the reaction between $\cdot SO_4^-$ and excess $S_2O_8^{2-}$. Therefore, a persulfate concentration of 0.3 g L^{-1} was chosen as the optimal reaction condition based on cost and environmental considerations.

$$\cdot SO_4^- + SO_4^{\cdot -} \rightarrow S_2O_8^{2-} \quad (1)$$

$$\cdot SO_4^- + S_2O_8^{2-} \rightarrow SO_4^{2-} + S_2O_8^{\cdot -} \quad (2)$$

Effects of initial pH. Fig. 6a illustrates the degradation efficiency of TCE at different pH values. It was observed that pH had a significant impact on the degradation of organic pollutants by sulfate free radicals. To investigate this effect, we adjusted the pH of the solution using sulfuric acid and dipotassium hydrogen phosphate, resulting in pH values of 3, 9 and 11. It was observed that the degradation efficiency of TCE was lower than normal under extremely acidic or alkaline conditions. This can be attributed to the susceptibility of the $MnCo_2O_4$ spinel structure to collapse under highly acidic conditions, thereby reducing its catalytic activity. Similarly,

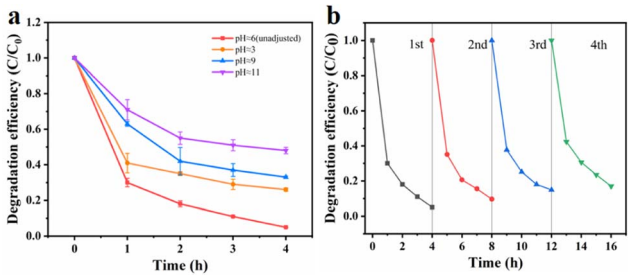

Fig. 6 Effect of reaction parameters on TCE degradation: initial pH value (a) and reusability of $MnCo_2O_4$/rGO as a catalyst activated PS for the degradation of TCE (b) [reaction conditions: PS dosage = 0.3 g L^{-1}, catalyst dosage = 0.3 g L^{-1} and reaction temperature = 25 °C].

under alkaline conditions, the reaction between $\cdot SO_4^-$ and OH^- leads to the formation of hydroxyl radicals with lower reactivity, shorter half-life, and diminished activation ability, as described in formula (3). Furthermore, when the pH exceeds 9, the decomposition of $MnCo_2O_4$ may occur, resulting in the formation of manganese and cobalt hydroxides, which in turn affects the degradation efficiency of trichloroethylene. Therefore, a pH of approximately 6 was determined as the optimal reaction condition for this experiment.

$$\cdot SO_4^- + OH^- \rightarrow SO_4^{2-} + OH^\cdot \quad (3)$$

$$\cdot SO_4^- + H_2O \rightarrow HSO_4^- + OH^\cdot \quad (4)$$

$$OH^\cdot + OH^\cdot \rightarrow H_2O_2 \quad (5)$$

$$S_2O_8^{2-} + H_2O_2 \rightarrow 2SO_4^{2-} + O_2 + 2H^+ \quad (6)$$

Reusability and stability of $MnCo_2O_4$/rGO catalyst. The cyclic performance of the $MnCo_2O_4$/rGO catalyst was assessed through a series of experiments. After each reaction, the catalyst was collected by centrifugation, followed by washing with ethanol and DI water, and subsequent drying in an oven. The treated catalyst was then reintroduced into the solution under identical conditions as the initial experiment for a second degradation experiment. This process was repeated three times to investigate any variations in the catalytic efficiency of the catalyst after each reaction. Fig. 6b demonstrates that even after three consecutive reactions, the degradation efficiency of trichloroethylene only decreased to 83% by the fourth reaction. This decrease in activity can be attributed to the consumption and leaching of metal ions into the solution during the reaction, as well as the absorption of certain reaction intermediates by the material. These factors result in a reduction in available catalytic active sites and the partial deterioration of the material structure after multiple reactions.[35]

Degradation mechanism of TCE

XPS characterization of $MnCo_2O_4$/rGO. It is considered that the catalytic process may cause the changes in the elemental valence of the catalyst, thus it is necessary to evaluate the surface properties of $MnCo_2O_4$/rGO after the reaction. Fig. 7 shows the changes of the valence states of the main elements of the material before and after the reaction. The survey spectrum of the sample is presented in Fig. 7a, indicating the primary chemical compositions of C, O, Mn, and Co elements. In Fig. 7b, the Co 2p spectrum shows two main photoelectron peaks, with binding energies of 780.0 eV and 795.3 eV, corresponding to the binding energies of Co 2p 3/2 and Co 2p 1/2 spin–orbit splitting. The peaks at 786.9 eV and 803.4 eV correspond to satellite peaks of Co 2p 3/2 and Co 2p 1/2. After the reaction, the content of Co^{3+} at the Co 2p 3/2 spin–orbit decreases from 48.1% to 44.4%. In contrast, the content of Co^{2+} increased from 51.8% to 55.6%. The Co^{2+} content at the Co 2p 1/2 spin–orbit decreases from 70.2% to 67.8%, and the Co^{3+} content increases accordingly. In Fig. 7c, there are also two main photoelectron peaks in the spectrum of Mn 2p, whose binding energies are 642.5 eV and 653.7 eV, corresponding to the binding energies of Mn 2p 3/2 and Mn 2p 1/2 spin–orbit splitting. After the reaction, the Mn^{3+} content at the 2p 3/2 spin–orbit of Mn increases from 43.3% to 52.5%, and the Mn^{2+} content decreases from 56.7% to 47.5%. The Mn^{3+} content at the Mn 2p 1/2 spin–orbit increases from 51.4% to 63.3%, and the Mn^{2+} content also changes, which indicates that the Mn(II) and Co(III) on the surface of the catalyst are partially converted to Mn(III) and Co(II). This provides a practical basis for the existence of Mn^{3+}/Mn^{2+} and Co^{3+}/Co^{2+} REDOX pairs.[37] In Fig. 7d, the peak type of C 1 s peak did not change significantly before and after the reaction, and the three peaks centered at 284.8, 286.3 and 288.6 eV corresponded to C–C, C–O and C=O. Based on the XPS characterization results and previous studies, it is proved that the process of $MnCo_2O_4$/rGO on persulfate activation involves the bimetallic synergistic effect of Mn(II)/Mn(III) and Co(III)/Co(II) REDOX electric pair in the material, resulting in higher catalytic activity.[38]

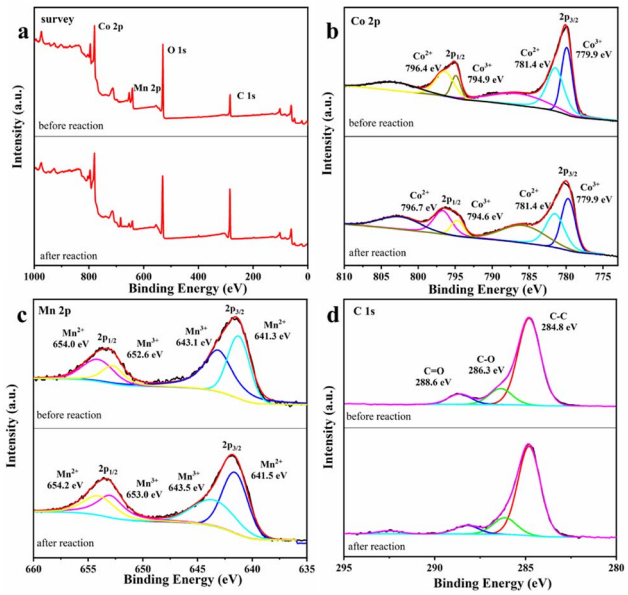

Fig. 7 XPS spectrum of (a) survey (b), Co 2p (c) Mn 2p and (d) C 1s of $MnCo_2O_4$/rGO before and after the reaction.

Free radical scavenging experiments and effect of metal ion leaching rate. To investigate the catalytic mechanism and identify the active species in the $MnCo_2O_4$/rGO/PS system, quenching experiments were performed by adding various radical scavengers. As reported in previous studies, $\cdot SO_4^-$ and OH· are critical for most transition metal activated PS systems.[17,39,40] Ethanol (EtOH) was selected for $\cdot SO_4^-$ scavenging, and *tert*-butanol (TBA) was chosen for OH· quenching. As depicted in Fig. 8, the removal efficiency of TCE was significantly reduced from 95% to 44.1% and 58.8% when 300 mM EtOH and 300 mM TBA were added to the TCE solution, confirming that $\cdot SO_4^-$ and OH· are the primary active species in the system. To ensure that the material does not cause secondary pollution to the environment, the leaching of metal ions into the solution was tested using ICP-MS. After adding 0.3 g L^{-1} of the catalyst for 4 h, the concentration of cobalt ion in the solution was 0.211 mg L^{-1}, and the concentration of manganese ion was 0.273 mg L^{-1}, meeting China's industrial pollutant emission standards. Under the same conditions with the $MnCo_2O_4$ catalyst, the concentration of cobalt ion in the solution was about 0.665 mg L^{-1}, and the concentration of manganese ion was 1.000 mg L^{-1}.

To investigate the catalytic mechanism and identify the active species in the $MnCo_2O_4$/rGO/PS system, quenching experiments were performed by adding various radical scavengers. As reported in previous studies, $\cdot SO_4^-$ and OH· are critical for most transition metal activated PS systems.[17,39,40] Ethanol (EtOH) was selected for $\cdot SO_4^-$ scavenging, and *tert*-butanol (TBA) was chosen for OH· quenching. As depicted in Fig. 8, the removal efficiency of TCE was significantly reduced from 95% to 44.1% and 58.8% when 300 mM EtOH and 300 mM TBA were added to the TCE solution, confirming that $\cdot SO_4^-$ and OH· are the primary active species in the system. To ensure that the material does not cause secondary pollution to the environment, the leaching of metal ions into the solution was tested using ICP-MS. After adding 0.3 g L^{-1} of the catalyst for 4 h, the concentration of cobalt ion in the solution was 0.211 mg L^{-1}, and the concentration of manganese ion was 0.273 mg L^{-1}, meeting China's industrial pollutant emission standards.

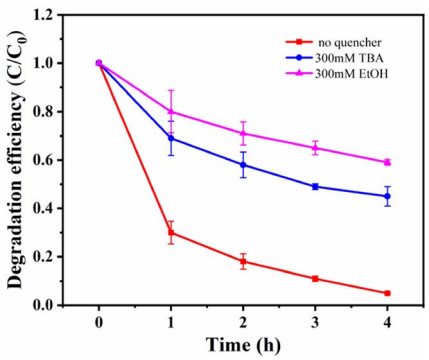

Fig. 8 Effects of different radical quencher for the TCE degradation in $MnCo_2O_4$/rGO/PS system [reaction conditions: PS dosage = 0.3 g L^{-1}, catalyst dosage = 0.3 g L^{-1}, reaction temperature = 25 °C and initial pH value = 6 (unadjusted)].

Under the same conditions with the $MnCo_2O_4$ catalyst, the concentration of cobalt ion in the solution was about 0.665 mg L^{-1}, and the concentration of manganese ion was 1.000 mg L^{-1}, confirming that rGO can serve as a carrier to reduce the overflow of metal ions in the catalyst. These results demonstrate that the leaching of metal ions during the reaction has a negligible impact on the reaction.

Reaction mechanisms. Based on the previous XPS analysis and free radical scavenging experiments, the possible catalytic process for the degradation of TCE by $MnCo_2O_4$/rGO/PS system was proposed. As shown in Fig. 9, this process consists of two parts: surface adsorption and free radical generation reaction. Firstly, $MnCo_2O_4$/rGO and PS are added to TCE solution to adsorb pollutants on rGO through interface effect, which is conducive to subsequent electron transfer. At the same time, Mn^{2+} and Co^{3+} on the surface of the catalyst will combine with PS to form $\cdot SO_4^-$, and part of $\cdot SO_4^-$ will react with H_2O to form OH·, which will further participate in the degradation process. These two free radicals will further participate in the degradation process. At the same time, part of the Mn^{3+} generated during the reaction will be reduced to Mn^{2+} by $\cdot SO_4^-$, and the other part will continue to react with the Co^{2+} generated by the reaction to form Mn^{2+} and Co^{3+}. This equilibrium will continue until PS is exhausted, as shown in eqn (7)–(11).[41,42] Furthermore, the synergistic effect of charge transfers between Co^{2+}/Co^{3+} and Mn^{2+}/Mn^{3+} redox pairs in $MnCo_2O_4$ can also accelerate the electron transfer efficiency, improve the activation efficiency, and promote the generation of free radicals. The standard oxidation–reduction potential of Co^{3+}/Co^{2+} was 1.92 V, while that of Mn^{3+}/Mn^{2+} was 1.51 V, which corroborated that the reduction of Co^{3+} by Mn^{2+} was thermodynamically feasible (eqn (12)).

$$Mn^{2+} + S_2O_8^{2-} \rightarrow Mn^{3+} + \cdot SO_4^- + SO_4^{2-} \quad (7)$$

$$Co^{2+} + S_2O_8^{2-} \rightarrow Co^{3+} + \cdot SO_4^- + SO_4^{2-} \quad (8)$$

$$H_2O + SO_4^{\cdot -} \rightarrow H^+ + OH\cdot + SO_4^{2-} \quad (9)$$

$$\cdot SO_4^- \text{ (absorbed)} \rightarrow \cdot SO_4^- \text{ (free)} \quad (10)$$

$$Mn^{3+} + SO_4^{\cdot -} \rightarrow Mn^{2+} + SO_4^{2-} \quad (11)$$

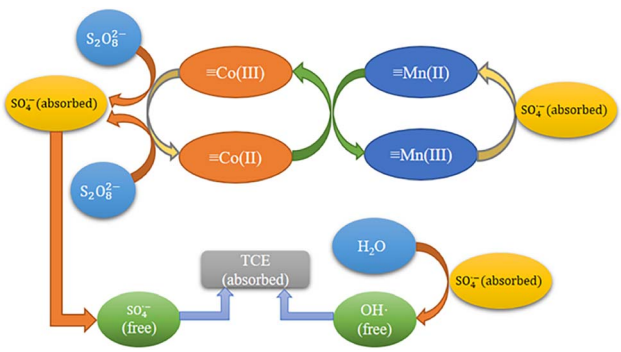

Fig. 9 Reaction mechanism of $MnCo_2O_4$/rGO activated PS.

$$Co^{3+} + Mn^{2+} \rightarrow Co^{2+} + Mn^{3+} \quad (12)$$

To gain deeper insights into the correlation between the properties of the synthesized $MnCo_2O_4$/RGO composites and their catalytic activities, we conducted first-principles simulations to investigate the interface between $CoMn_2O_4$ and rGO. Detailed information regarding the calculations can be found in the experimental section. Typically, when two materials come into contact, a Schottky electric field arises due to their disparate work functions.[43] In our study, the calculated work functions of $MnCo_2O_4$ (311) and rGO were determined to be 5.487 eV and 4.456 eV, respectively (Fig. S1†). This discrepancy implies that free electrons will migrate from rGO to $MnCo_2O_4$ at the interface until the Fermi levels align (Fig. S2†). As a result, $MnCo_2O_4$ acquires a negative charge in equilibrium, while rGO exhibits a positive charge near its surface owing to the injection of electrons from rGO into $MnCo_2O_4$. Furthermore, the electric field between $MnCo_2O_4$ and rGO remains unscreened due to the low carrier density in the $MnCo_2O_4$ semiconductor. Consequently, an accumulation of free electrons occurs near the surface of $MnCo_2O_4$. This observation is also supported by the charge density difference at the $MnCo_2O_4$ (311)/rGO interface. As illustrated in Fig. S3,† a discernible increase in electron density (depicted by the green color) is observed at the $MnCo_2O_4$ surface, while a decrease in electron density is observed at the rGO surface (depicted by the blue color). Consequently, the abundant electrons in $MnCo_2O_4$ facilitate the activation of persulfate through the Co(III)/Co(II) and Mn(III)/Mn(II) redox cycles, which in turn provided electrons for PS to break the O–O bond in its molecule, generating $SO_4^{\bullet -}$ species. Notably, the built-in electric field electron transfer from rGo to $MnCo_2O_4$ promoted the reduction of Co(III) and Mn(III) and ensured the continuous production of $SO_4^{\bullet -}$.

Possible degradation pathways of TCE. The reaction intermediates of TCE degradation were identified by GC-MS (Fig. S4†). The retention time of the intermediates is 8.17 min. Compared with the standard spectrogram, the intermediate product is dichloromethane (CH_2Cl_2), and a small amount of ethyl acetoacetate ($C_6H_{10}O_3$) is generated. It can be inferred from the report that the degradation path of TCE may be to break the double bond through addition reaction to generate chloroform ($CHCl_3$), then dechlorinate to form dichloromethane (CH_2Cl_2),[44] and finally mineralize to H_2O and CO_2.[45,46] The degradation path is shown in Fig. 10.

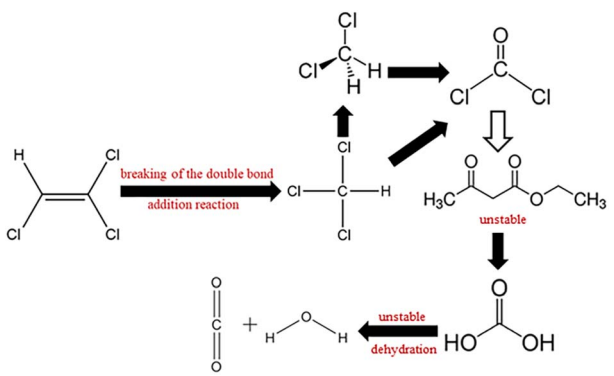

Fig. 10 Possible degradation pathways of TCE.

Conclusions

In summary, $MnCo_2O_4$/rGO nanocomposites were prepared by two-step solvothermal method and it was then used as catalyst to activate PS toward the degradation of TCE. The effects of different rGO loads on degradation efficiency were discussed. Compared with bare $MnCo_2O_4$, $MnCo_2O_4$/rGO composite was more stable and has stronger activation performance for PS. The degradation efficiency of trichloroethylene can reach 95% within 4 h without changing the initial pH value. The leaching rate of metal ions after the reaction suggests that the leaching of metal ions during the reaction process has little impact on the environment. The explanation mechanism in the reaction process was studied by XPS analysis and free radical scavenging experiment, and it was proved that $\cdot SO_4^-$ and OH· were both present and active. In addition, the degradation path of TCE was verified by GC/MS. The results showed that the degradation path was a bond breaking dechlorination process, with dichloromethane (CH_2Cl_2) and a small amount of ethyl acetoacetate ($C_6H_{10}O_3$) as its intermediate products, and finally mineralized into H_2O and CO_2. All the results show that $MnCo_2O_4$/rGO nanocomposite is an efficient catalyst and can be widely used in the degradation of pollutants in the environment.

Author contributions

All authors contributed to the study conception and design. Material preparation, data collection and analysis were performed by Lu Zhang, Pengfei Ji, Rui Song, Jiayuan Li, Kaifeng Qin and Gang Xu. The first draft of the manuscript was written by Lu Zhang and all authors commented on previous versions of the manuscript. All authors read and approved the final manuscript.

Conflicts of interest

There are no conflicts to declare.

Acknowledgements

We thank all participants for their cooperation and support. We are grateful for the technical support provided by the School of Environmental and Chemical Engineering of Shanghai University. This work was supported by the National Natural Science Foundation of China (No. 11975147 and 12175133), and National Key Research and Development Project (No. 2021YFC1808902, 2020YFC1808203).

References

1 K. Ohlen, Y. K. Chang, W. Hegemann, C. R. Yin and S. T. Lee, *Chemosphere*, 2005, **58**, 373–377.

2 B. Bakke, P. A. Stewart and M. A. Waters, *J. Occup. Environ. Hyg.*, 2007, **4**, 375–390.
3 K. M. Gilbert, B. Przybyla, N. R. Pumford, T. Han, J. Fuscoe, L. K. Schnackenberg, R. D. Holland, J. C. Doss, L. A. MacMillan-Crow and S. J. Blossom, *Chem. Res. Toxicol.*, 2009, **22**, 626–632.
4 T. Alapi and A. Dombi, *Chemosphere*, 2007, **67**, 693–701.
5 S. D. Justicia-Leon, S. Higgins, E. E. Mack, D. R. Griffiths, S. Q. Tang, E. A. Edwards and F. E. Loffler, *Environ. Sci. Technol.*, 2014, **48**, 1851–1858.
6 B. Z. Li, K. F. Lin, W. Zhang, S. G. Lu and Y. D. Liu, *J. Environ. Eng.*, 2012, **138**, 903–914.
7 S. Randazzo, O. Scialdone, E. Brillas and I. Sires, *J. Hazard. Mater.*, 2011, **192**, 1555–1564.
8 Z. S. Wei and Y. Seo, *J. Hazard. Mater.*, 2010, **181**, 147–153.
9 J. S. Yang, K. Baek, T. S. Kwon and J. W. Yang, *J. Ind. Eng. Chem.*, 2009, **15**, 777–779.
10 Y. Miyake, A. Sakoda, H. Yamanashi, H. Kaneda and M. Suzuki, *Water Res.*, 2003, **37**, 1852–1858.
11 F. Berrelleza-Valdez, J. Parades-Aguilar, C. E. Pena-Limon, M. T. Certucha-Barragan, N. Gamez-Meza, D. Serrano-Palacios, L. A. Medina-Juarez and K. Calderon, *J. Environ. Manage.*, 2019, **241**, 211–218.
12 A. Siggins, A. M. Enright and V. O'Flaherty, *Water Res.*, 2011, **45**, 4035–4046.
13 M. Ahmad, S. S. Lee, A. U. Rajapaksha, M. Vithanage, M. Zhang, J. S. Cho, S. E. Lee and Y. S. Ok, *Bioresour. Technol.*, 2013, **143**, 615–622.
14 W. S. Koe, J. W. Lee, W. C. Chong, Y. L. Pang and L. C. Sim, *Environ. Sci. Pollut. Res.*, 2020, **27**, 2522–2565.
15 A. Baldermann, S. Kaufhold, R. Dohrmann, C. Baldermann, I. Letofsky-Papst and M. Dietzel, *Chemosphere*, 2021, **282**, 131018.
16 M. Priyadarshini, I. Das, M. M. Ghangrekar and L. Blaney, *J. Environ. Manage.*, 2022, **316**, 115295.
17 S. Waclawek, H. V. Lutze, K. Grubel, V. V. T. Padil, M. Cernik and D. D. Dionysiou, *Chem. Eng. J.*, 2017, **330**, 44–62.
18 P. Hu and M. Long, *Appl. Catal., B*, 2016, **181**, 103–117.
19 Y. F. Ji, W. P. Xie, Y. Fan, Y. Y. Shi, D. Y. Kong and J. H. Lu, *Chem. Eng. J.*, 2016, **286**, 16–24.
20 R. L. Johnson, P. G. Tratnyek and R. O. Johnson, *Environ. Sci. Technol.*, 2008, **42**, 9350–9356.
21 A. Ghauch, A. M. Tuqan and N. Kibbi, *Chem. Eng. J.*, 2012, **197**, 483–492.
22 R. C. Zhang, P. Z. Sun, T. H. Boyer, L. Zhao and C. H. Huang, *Environ. Sci. Technol.*, 2015, **49**, 3056–3066.
23 W. S. Chen and Y. C. Su, *Ultrason. Sonochem.*, 2012, **19**, 921–927.
24 J. Criquet and N. K. V. Leitner, *Chem. Eng. J.*, 2011, **169**, 258–262.
25 Y. Lei, C. S. Chen, Y. J. Tu, Y. H. Huang and H. Zhang, *Environ. Sci. Technol.*, 2015, **49**, 6838–6845.
26 Y. B. Ding, L. H. Zhu, N. Wang and H. Q. Tang, *Appl. Catal., B*, 2013, **129**, 153–162.
27 G. P. Anipsitakis and D. D. Dionysiou, *Environ. Sci. Technol.*, 2003, **37**, 4790–4797.
28 J. Fernandez, P. Maruthamuthu, A. Renken and J. Kiwi, *Appl. Catal., B*, 2004, **49**, 207–215.
29 X. Y. Chen, J. W. Chen, X. L. Qiao, D. G. Wang and X. Y. Cai, *Appl. Catal., B*, 2008, **80**, 116–121.
30 S. Muhammad, E. Saputra, H. Q. Sun, J. D. Izidoro, D. A. Fungaro, H. M. Ang, M. O. Tade and S. B. Wang, *RSC Adv.*, 2012, **2**, 5645–5650.
31 G. S. Wang, Y. Y. Ma, Y. Tong and X. F. Dong, *J. Ind. Eng. Chem.*, 2017, **48**, 142–150.
32 T. Zhu, S. C. Chang, Y. F. Song, M. Lahoubi and W. Wang, *Chem. Eng. J.*, 2019, **373**, 755–766.
33 G. Jayalakshmi, K. Saravanan, T. Arun, K. Suresh, B. Sundaravel, B. K. Panigrahi and D. Kanjilal, *Carbon*, 2017, **119**, 172–178.
34 P. L. Meena, S. Pal, K. Sreenivas and R. Kumar, *Adv. Sci. Lett.*, 2015, **21**, 2760–2763.
35 Y. J. Yao, Z. H. Yang, D. W. Zhang, W. C. Peng, H. Q. Sun and S. B. Wang, *Ind. Eng. Chem. Res.*, 2012, **51**, 6044–6051.
36 P. L. Hao, M. Z. Hu, R. Xing and W. J. Zhou, *J. Alloys Compd.*, 2020, **823**, 153757.
37 X. Y. Wang, J. J. Jiang, Y. H. Ma, Y. Y. Song, T. R. Li and S. S. Dong, *J. Colloid Interface Sci.*, 2021, **600**, 449–462.
38 N. H. Trang, E. Kwon, G. Lisak, C. Hu and K. Y. A. Lin, *Chemosphere*, 2021, **267**, 128906.
39 Z. Zhou, X. Liu, K. Sun, C. Lin, J. Ma, M. He and W. Ouyang, *Chem. Eng. J.*, 2019, **372**, 836–851.
40 S. Wacławek, H. V. Lutze, K. Grübel, V. V. T. Padil, M. Černík and D. D. Dionysiou, *Chem. Eng. J.*, 2017, **330**, 44–62.
41 Q. Z. Ni, J. F. Ma, C. H. Fan, Y. Kong, M. G. Peng and S. Komarneni, *Ceram. Int.*, 2018, **44**, 19474–19480.
42 J. Deng, Y. Q. Cheng, Y. A. Lu, J. C. Crittenden, S. Q. Zhou, N. Y. Gao and J. Li, *Chem. Eng. J.*, 2017, **330**, 505–517.
43 C. Zhang, X. P. Geng, S. L. Tang, M. S. Deng and Y. W. Du, *J. Mater. Chem. A*, 2017, **5**, 5912–5919.
44 H. R. Dong, K. J. Hou, W. W. Qiao, Y. J. Cheng, L. H. Zhang, B. Wang, L. Li, Y. Y. Wang, Q. Ning and G. M. Zeng, *Chem. Eng. J.*, 2019, **359**, 1046–1055.
45 T. Chang, C. L. Ma, A. Nikiforov, S. K. P. Veerapandian, N. De Geyter and R. Morent, *J. Phys. D: Appl. Phys.*, 2022, **55**, 125202.
46 M. Ali, M. Danish, M. Tariq, A. Ahmad, K. S. Ayub and S. G. Lyu, *Chem. Eng. J.*, 2020, **399**, 125754.